PROCEEDINGS OF SPIE

SPIEDigitalLibrary.org/conference-proceedings-of-spie

Implicit electric field conjugation for improved starlight rejection through a single-mode fiber

Joshua Liberman, Jorge Llop-Sayson, Arielle Bertrou-Cantou, Dimitri Mawet, A.J. Eldorado Riggs, et al.

Joshua Liberman, Jorge Llop-Sayson, Arielle Bertrou-Cantou, Dimitri Mawet, A.J. Eldorado Riggs, Niyati Desai, "Implicit electric field conjugation for improved starlight rejection through a single-mode fiber," Proc. SPIE 12680, Techniques and Instrumentation for Detection of Exoplanets XI, 126802D (5 October 2023); doi: 10.1117/12.2677532

SPIE.

Event: SPIE Optical Engineering + Applications, 2023, San Diego, California, United States

Implicit electric field conjugation for improved starlight rejection through a single-mode fiber

Joshua Liberman[a, b], Jorge Llop-Sayson[a], Arielle Bertrou-Cantou[a], Dimitri Mawet[a,c], A J Eldorado Riggs[c], and Niyati Desai[a]

[a]California Institute of Technology, Pasadena, California, United States
[b]James C. Wyant College of Optical Sciences, University of Arizona, Meinel Building 1630 E. University Blvd., Tucson, AZ. 85721
[c]Jet Propulsion Laboratory, California Institute of Technology, Pasadena, California, United States

ABSTRACT

Connecting a coronagraph instrument to a spectrograph via a single-mode optical fiber is a promising technique for characterizing the atmospheres of exoplanets with ground and space-based telescopes. However, due to the small separation and extreme flux ratio between planets and their host stars, instrument sensitivity will be limited by residual starlight leaking into the fiber. To minimize stellar leakage, we must control the electric field at the fiber input. Implicit electric field conjugation (iEFC) is a model-independent wavefront control technique in contrast with classical electric field conjugation (EFC) which requires a detailed optical model of the system. We present here the concept of an iEFC-based wavefront control algorithm to improve stellar rejection through a single-mode fiber. As opposed to image-based iEFC which relies on minimizing intensity in a dark hole region, our approach aims to minimize the amount of residual starlight coupling into a single-mode fiber. We present broadband simulation results demonstrating a normalized intensity $\geq 10^{-10}$ for both fiber-based EFC and iEFC. We find that both control algorithms exhibit similar performance for the low wavefront error case, however, iEFC outperforms EFC by $\approx$ 100x in the high wavefront error regime. Having no need for an optical model, this fiber-based approach is theoretically easier to implement than conventional EFC on future ground and space-based telescope missions.

Keywords: exoplanets, high contrast imaging, wavefront sensing, wavefront control, single-mode fibers, spectroscopy

1. INTRODUCTION

Direct imaging is a valuable technique for the detection and characterization of exoplanets.[1,2] However, imaging Earth-like planets around Sun-like stars remains a significant challenge due to the strict wavefront stability requirements set by future space-based telescopes, such as the Habitable Worlds Observatory (see also the Habitable Exoplanet Observatory (HabEx) and the Large UV/Optical/IR Surveyor (LUVOIR) concepts[3,4]). Detecting exo-Earths will require raw contrasts of $\simeq 10^{-10}$ at a close angular separation of ≈ 0.1".[1]

Fiber-fed spectroscopy allows for the detection of planets, using precision radial velocity measurements.[5] Connecting a coronagraph to a medium-to-high resolution spectrograph via an optical fiber, known as high dispersion coronagraphy (HDC), enables rejection of starlight at small inner working angles.[6,7] Furthermore, HDC can be used to measure planetary orbital velocities and atmospheric compositions. Modern instruments such as the Keck Planet Imager and Characterizer (KPIC) and the Subaru Telescope's Rigorous Exoplanetary Atmosphere Characterization with High dispersion coronography (REACH) demonstrate the feasibility of HDC on diffraction-limited telescopes by coupling planet light into a single-mode fiber (SMF).[8,9] The SMF further

Further author information: (Send correspondence to Joshua Liberman)
Joshua Liberman: E-mail: jliberman@arizona.edu

Techniques and Instrumentation for Detection of Exoplanets XI, edited by Garreth J. Ruane, Proc. of SPIE Vol. 12680, 126802D · © 2023 SPIE
0277-786X · doi: 10.1117/12.2677532

rejects starlight due to its mode selectivity.[10,11] However, despite the increased stellar rejection, the signal-to-noise ratio (SNR) of the planet spectrum remains limited due to residual starlight leaking into the fiber. This leakage results in excess photon noise and contaminates the planet signal.[12,13]

Combining wavefront control techniques and adaptive optics, stellar speckles can be suppressed and planet signal can be recovered. In wavefront control, one or two deformable mirrors (DM) modify the incoming electric field to create a dark hole (DH) region, free of speckles.[10] While many wavefront control techniques exist,[14] Electric Field Conjugation (EFC) is often used due to its superior performance relative to most other controllers.[15] Additionally, EFC is the primary controller for the Nancy Grace Roman Space Telescope.[16] EFC involves minimizing the focal plane electric field, using an optimal DM shape. The DM pattern is derived from a detailed instrument model.[14,17]

The model-dependency of EFC limits its feasibility on-sky, as any telescope system instabilities will reduce the algorithm's effectiveness.[14,18] Implicit EFC (iEFC) utilizes a linear response between the DM and modulated intensity measurements, such that the reconstructed electric field is no longer computed explicitly.[14,19,20] In this work, we propose an algorithm based on iEFC to minimize the speckles coupling into a SMF. In Section 2, we derive the equations for fiber-based iEFC. In Section 3, we describe our simulation results, and in Section 4, we discuss and conclude our work.

2. THEORY

2.1 EFC With a Single-Mode Fiber

We begin by expressing the measured intensity at the output of the single-mode fiber (SMF) as an overlap integral. We wish to determine how well the output field of the beam, E_{im}, overlaps with the fiber's fundamental mode shape, denoted by Ψ_{SMF}. Thus, the overlap integral can be expressed as

$$I \propto \left| \int E_{im} \Psi_{SMF} da \right|^2 \tag{1}$$

where da represents the differential area element in the image plane.

To measure E_{im}, we use the common method of pairwise probes described in Ref. 21 with the resolution element defined as the overlap integral for the SMF.[10]

We assume a linear relationship between the DM actuators and the electric field in the image plane* (see Section A for the full derivation). This, in turn, allows us to calculate the DM shape that minimizes the overlap integral, and in turn, the intensity in the DH region. Further details on the minimization procedure can be found in Ref. 10. Ultimately, our minimization solution can be expressed as

$$\vec{u} = -\mathbf{G}^{\dagger} \hat{s} \tag{2}$$

where $\vec{u}$ is the DM solution that will minimize the light coupling into the SMF, $\mathbf{G}$ is the model-based Jacobian, accounting for the effect of each actuator on the overlap integral,[10] and $\hat{s}$ is the estimate of our overlap integral.

2.2 iEFC With a Single-Mode Fiber

Let us introduce a vector of Fourier modes, denoted by $\vec{\alpha}$. Now, we can define the probe and mode intensities as I_u and I_α, respectively. Additionally, we define $\mathbf{G_u}$ as the effect of each actuator on the overlap integral and $\mathbf{G}_\alpha$ as the effect of each Fourier mode on the overlap integral. With I_u defined in Ref. 10 as

$$I_u = \left| \int (E_{ab} + \mathbf{G_u} \vec{u}) \Psi_{SMF} da \right|^2$$

, we can express the mode intensity as $I_\alpha = \left| \int (\vec{E_{ab}} + \mathbf{G}_\alpha \vec{\alpha}) \Psi_{SMF} da \right|^2$. Combining I_u and I_α we obtain a general expression for the intensity:

*Note that the method of EFC breaks down when this linear assumption no longer holds. This is particularly relevant in on-sky applications when ϕ_{DM} and ϕ_{ab} are no longer $<< 1$.

$$I_{u,\alpha} = \left| \int (\vec{E_{ab}} \pm \mathbf{G_u}\vec{u} \pm \mathbf{G}_\alpha \vec{\alpha}) \Psi_{SMF} da \right|^2 \tag{3}$$

.

Now, the DH intensity can be characterized as a double-difference between I_u and I_α. Thus, for a given mode α_i, the positive and negative probe/mode intensities can be expressed as

$$\begin{aligned} I_{u+,\alpha_i+} = &\left| \int \Psi_{SMF} \vec{E_{ab}} da \right|^2 + \left| \int \Psi_{SMF} \mathbf{G_u} \vec{u} da \right|^2 + \left| \int \Psi_{SMF} \mathbf{G}_\alpha \vec{\alpha} da \right|^2 \\ &+2Re\left\{ \int \Psi_{SMF} \vec{E_{ab}} da \times \int \Psi_{SMF} \mathbf{G_u} \vec{u} da \right\} \\ &+2Re\left\{ \int \Psi_{SMF} \vec{E_{ab}} da \times \int \Psi_{SMF} \mathbf{G}_\alpha \vec{\alpha} da \right\} \\ &+2Re\left\{ \int \Psi_{SMF} \mathbf{G_u} \vec{u} da \times \int \Psi_{SMF} \mathbf{G}_\alpha \vec{\alpha} da \right\} \end{aligned} \tag{4}$$

$$\begin{aligned} I_{u-,\alpha_i+} = &\left| \int \Psi_{SMF} \vec{E_{ab}} da \right|^2 + \left| \int \Psi_{SMF} \mathbf{G_u} \vec{u} da \right|^2 + \left| \int \Psi_{SMF} \mathbf{G}_\alpha \vec{\alpha} da \right|^2 \\ &-2Re\left\{ \int \Psi_{SMF} \vec{E_{ab}} da \times \int \Psi_{SMF} \mathbf{G_u} \vec{u} da \right\} \\ &+2Re\left\{ \int \Psi_{SMF} \vec{E_{ab}} da \times \int \Psi_{SMF} \mathbf{G}_\alpha \vec{\alpha} da \right\} \\ &-2Re\left\{ \int \Psi_{SMF} \mathbf{G_u} \vec{u} da \times \int \Psi_{SMF} \mathbf{G}_\alpha \vec{\alpha} da \right\} \end{aligned} \tag{5}$$

$$\begin{aligned} I_{u+,\alpha_i-} = &\left| \int \Psi_{SMF} \vec{E_{ab}} da \right|^2 + \left| \int \Psi_{SMF} \mathbf{G_u} \vec{u} da \right|^2 + \left| \int \Psi_{SMF} \mathbf{G}_\alpha \vec{\alpha} da \right|^2 \\ &+2Re\left\{ \int \Psi_{SMF} \vec{E_{ab}} da \times \int \Psi_{SMF} \mathbf{G_u} \vec{u} da \right\} \\ &-2Re\left\{ \int \Psi_{SMF} \vec{E_{ab}} da \times \int \Psi_{SMF} \mathbf{G}_\alpha \vec{\alpha} da \right\} \\ &-2Re\left\{ \int \Psi_{SMF} \mathbf{G_u} \vec{u} da \times \int \Psi_{SMF} \mathbf{G}_\alpha \vec{\alpha} da \right\} \end{aligned} \tag{6}$$

$$\begin{aligned} I_{u-,\alpha_i-} = &\left| \int \Psi_{SMF} \vec{E_{ab}} da \right|^2 + \left| \int \Psi_{SMF} \mathbf{G_u} \vec{u} da \right|^2 + \left| \int \Psi_{SMF} \mathbf{G}_\alpha \vec{\alpha} da \right|^2 \\ &-2Re\left\{ \int \Psi_{SMF} \vec{E_{ab}} da \times \int \Psi_{SMF} \mathbf{G_u} \vec{u} da \right\} \\ &-2Re\left\{ \int \Psi_{SMF} \vec{E_{ab}} da \times \int \Psi_{SMF} \mathbf{G}_\alpha \vec{\alpha} da \right\} \\ &+2Re\left\{ \int \Psi_{SMF} \mathbf{G_u} \vec{u} da \times \int \Psi_{SMF} \mathbf{G}_\alpha \vec{\alpha} da \right\} \end{aligned} \tag{7}$$

We then obtain the intensity differences for positive and negative modes:

$$\begin{aligned} \Delta I_{\alpha_i+} = &4Re\left\{ \int \Psi_{SMF} \vec{E_{ab}} da \times \int \Psi_{SMF} \mathbf{G_u} \vec{u} da \right\} \\ &+4Re\left\{ \int \Psi_{SMF} \mathbf{G_u} \vec{u} da \times \int \Psi_{SMF} \mathbf{G}_\alpha \vec{\alpha} da \right\} \end{aligned} \tag{8}$$

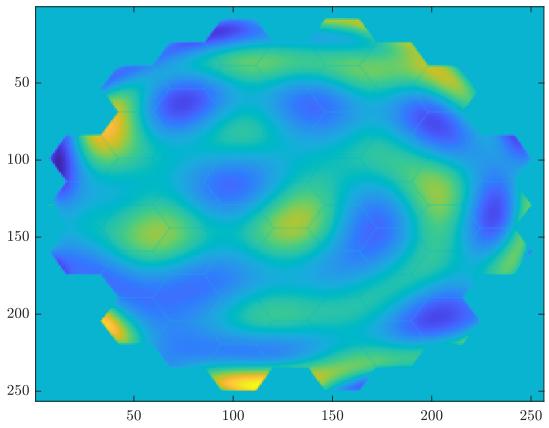

Figure 1. The LUVOIR-B phase map used in HCST simulations.

$$\begin{aligned}\Delta I_{\alpha_i -} = 4Re\left\{\int \Psi_{SMF}\vec{E_{ab}}da \times \int \Psi_{SMF}\mathbf{G_u}\vec{u}da\right\} \\ -4Re\left\{\int \Psi_{SMF}\mathbf{G_u}\vec{u}da \times \int \Psi_{SMF}\mathbf{G}_\alpha\vec{\alpha}da\right\}\end{aligned} \tag{9}$$

.

We now compute the difference between the two mode states, which we refer to as the double-difference measured intensity. In doing so, we obtain

$$\frac{\Delta\Delta I_{\alpha_i,u}}{2} = \frac{\Delta I_{\alpha_i +} - \Delta I_{\alpha_i -}}{2} = 4Re\left\{\int \Psi_{SMF}\mathbf{G_u}\vec{u}da \times \int \Psi_{SMF}\mathbf{G}_\alpha\vec{\alpha}da\right\} = F \tag{10}$$

where F is defined as our interaction matrix. Finally, we minimize the overlap integral (s) through the SMF, using an expression that directly relates the DM modes to the measured double-difference intensity:

$$\Delta I_u = Fs \tag{11}$$

where s can be obtained using a linear least-squares approximation.

3. SIMULATIONS

To assess performance of iEFC through a single-mode fiber (SMF), we developed an end-to-end optical simulation based on the current layout of the high contrast spectroscopy for segmented telescopes testbed (HCST).[22]

Our simulation was constructed with the Fast Linearized Coronagraph Optimizer (FALCO) package within MATLAB, which provides realistic optical propagations for coronagraphs and AO-based systems.[23] We simulated a segmented pupil, based on the LUVOIR-B design, with a circular aperture, a Lyot stop, a charge 6 Vector Vortex Coronagraph (VVC), a 34x34 actuator Boston Micromachines DM, and a single-mode fiber with a mode field radius of 0.507 λ/D. All simulations were computed around a central wavelength of $\lambda_0 = 750$ nm.

Realistic speckles were generated using a phase map spanning low-high spatial frequencies (nolls 4-100) with an RMS wavefront error of 10 nm–consistent with the aberrations we observe on our testbed.[22]

In defining contrast performance, we adopt the formalism of Ref. 10. We define SMF normalized intensity (NI) as the measured power at the output of the SMF divided by measured intensity at the output of the SMF centered on the non-coronagraphic stellar PSF.

We first simulate fiber-based iEFC and EFC at 2 different locations within our image, using a circular control region of 1 λ/D to match the dimensions of our fiber and a fixed configuration of 24 Fourier modes. The small control region gives us greater flexibility over the placement of our modes.

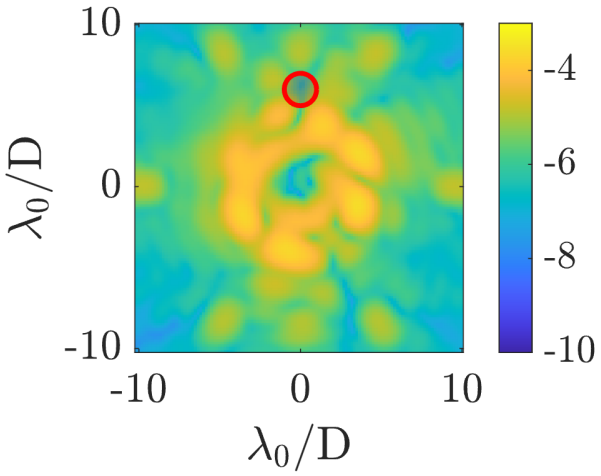

Figure 2. A simulated stellar PSF after correction with fiber-based iEFC. The red circle marks the position of the fiber at (0, 6) λ/D.

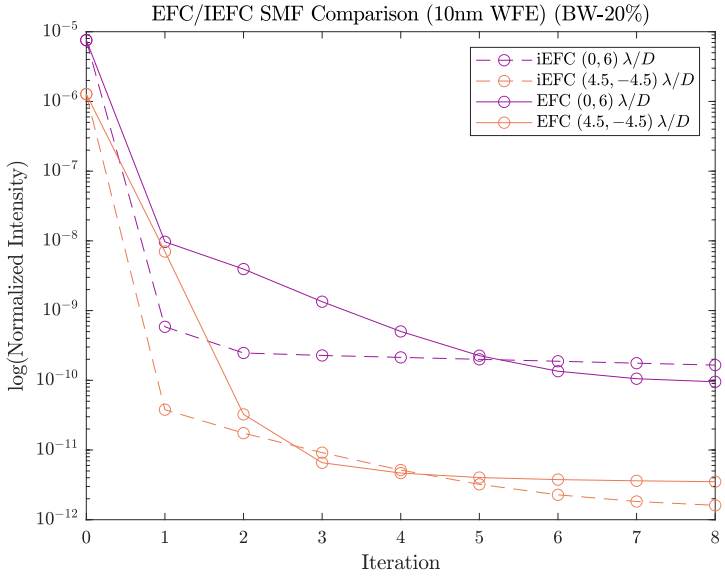

Figure 3. Contrast performance of EFC versus iEFC through a SMF at 2 different fiber locations.

A simulated stellar PSF is shown in Fig. 2. Note that fiber-based iEFC will not necessarily create a DH at a given fiber position, as it is minimizing the overlap integral rather than the electric field.[10] In Fig. 3, we compare performance of iEFC to that of EFC in polychromatic light with a $\Delta\lambda/\lambda = 20\%$ bandwidth and 9 sub-bandpasses.

All solutions converge on a NI of $\approx 10^{-10}$ or lower. We observe similar performance between EFC and iEFC, with both methods converging in fewer than 8 iterations. Our findings are consistent with those of Ref. 14. Additionally, we observe some variation in the NI as a function of the fiber position. This is to be expected, as the phase pattern of the electric field along the fiber tip, the orientation of the Fourier modes with respect to the fiber, and the wavefront error all result in variation of the NI.

We then simulate three different Fourier mode configurations at a fixed fiber location of (0, -8) λ/D. Fig 4 shows the Fourier modes overlaid on a 2-D projection of the fiber's fundamental mode. In Fig. 5, we compare the NI of EFC to that of iEFC for a varying number of Fourier modes and a bandwidth of $\Delta\lambda/\lambda = 30\%$. EFC

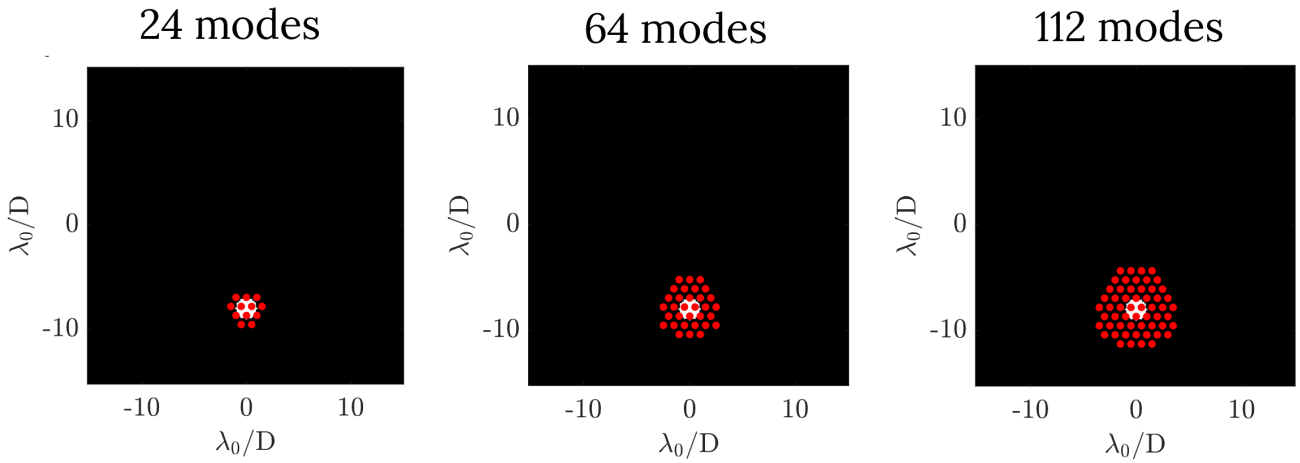

Figure 4. Three different Fourier mode configurations overlaid on a 2-D projection of the fiber's fundamental mode at (0, -8) λ/D.

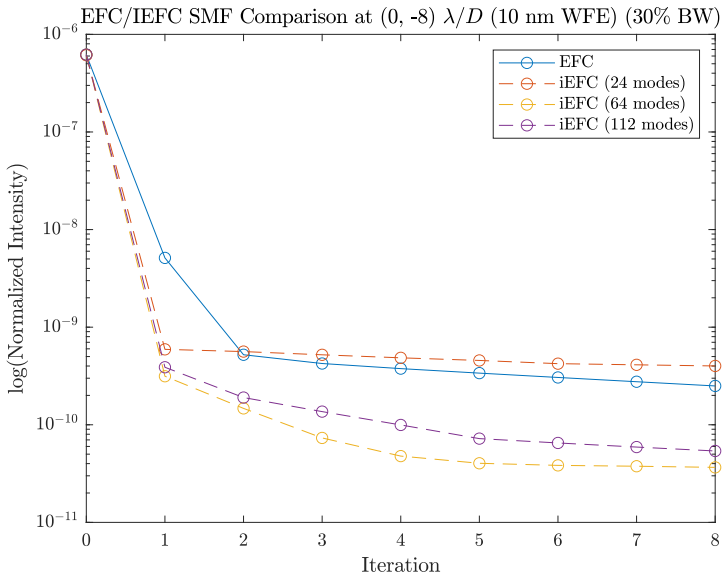

Figure 5. EFC versus iEFC contrast for a 30% bandwidth. iEFC performance is evaluated for three different mode configurations.

and iEFC again exhibit similar similar performance through the fiber, however, iEFC achieves higher contrasts (NI$\approx 10^{-11}$) as we increase the number of modes. The contrast improvement in iEFC for a greater number of Fourier modes is to be expected, as we are able to control a larger range of spatial frequencies by increasing the number of modes. Our simulation results are consistent with the explanation provided in Ref. 19, where the authors propose that the number of modes scales with the spatial frequency.

While we find that iEFC contrast improves with the number of Fourier modes, it is important to consider the increased Jacobian measurement time for iEFC in this analysis. In Fig. 6, we compare the time to construct the Jacobian in iEFC vs EFC at a $\Delta\lambda/\lambda = 20\%$ bandwidth with 9 sub-bandpasses. For EFC, the Jacobian construction time is obtained directly from our FALCO simulation. In iEFC, we estimate the Jacobian construction time, assuming 1-second integration times.

We observe that as the number of modes are increased, the time to construct the iEFC measurement Jacobian

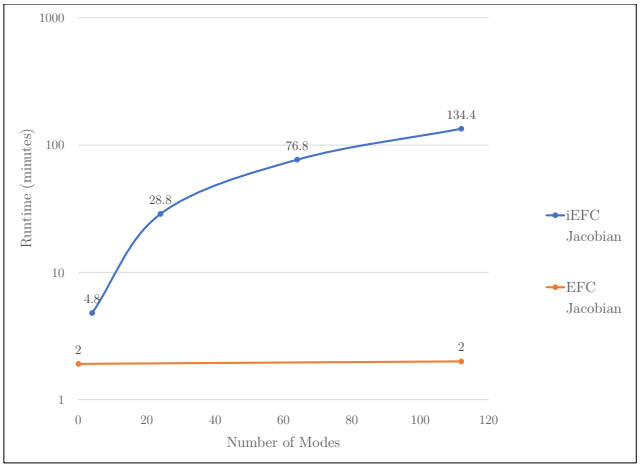

Figure 6. Time required to construct the Jacobian for iEFC vs EFC. In iEFC, the Jacobian measurement time scales with the number of modes.

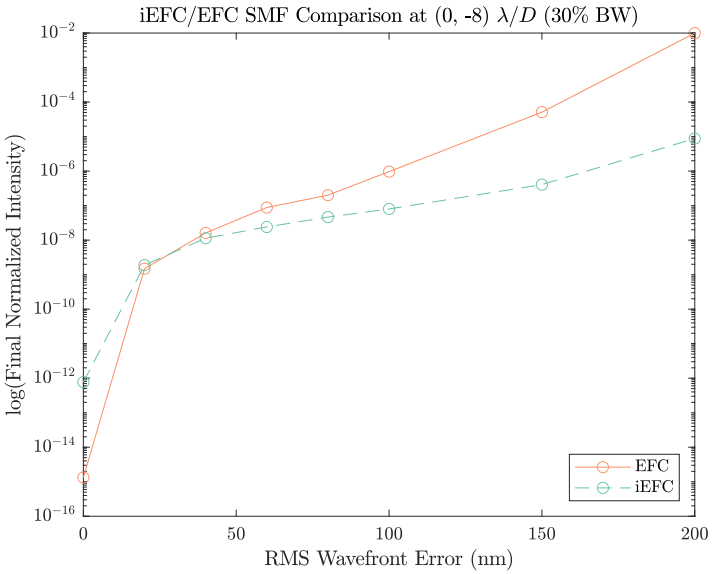

Figure 7. Final normalized intensity over a range of injected model errors.

increases significantly. On the other hand, the EFC Jacobian construction time remains fixed, as it is computed from a model with a fixed number of modes. iEFC's long Jacobian construction time, relative to that of EFC, poses a concern for future space-based imaging missions that will require a robust wavefront sensing and control loop to reach at least 10^{-10} contrast.[4]

In Fig. 7, we examine how EFC and iEFC respond to model errors within our simulation. As the WFE amplitude is increased, the contrast achieved with EFC decreases. This is consistent with what we expect as EFC computes a control solution from an ideal optical model. However, for iEFC in the high WFE regime, the solution remains fairly constant, with iEFC showing a ≈100x contrast improvement over EFC with 150 nm RMS WFE.

4. DISCUSSION AND CONCLUSION

We describe a new method of focal plane wavefront control through a SMF. The model-free approach in iEFC combined with the mode selectivity of a SMF provides a simple method of wavefront control at higher contrasts than that of conventional EFC or iEFC.[10,14]

In simulations, we consistently demonstrate broadband contrasts of at least 10^{-10} with a charge 6 VVC and observe similar performance between EFC and iEFC through the fiber. We also observe that iEFC is more flexible in its implementation. In EFC, every DM mode is used when computing the Jacobian, such that the algorithm attempts to correct spatial frequencies far from the control region. iEFC enables us to be more selective in our mode placement, using only the modes within a given radius of the fiber location. While we observe that a greater number of modes correlates with a higher contrast in iEFC, we eventually reach a point of diminishing returns for ≈ 112 modes, in which the algorithm fails to converge on an NI below 10^{-11}.

We also demonstrate that fiber-based iEFC is more resilient to model errors than fiber-based EFC. This is a particularly notable result, as EFC on ground-based telescopes is currently limited by the model-based Jacobian solution. Thus, high contrasts with fiber-based iEFC may be achievable on current and future fiber-fed spectrographs such as the Keck-KPIC, Keck-HISPEC, and TMT-MODHIS instruments.[8,24]

Future work will be needed to identify the optimal number of modes in our iEFC control implementation. Additionally, we plan on conducting fiber-based iEFC experiments using the fiber injection unit on Caltech's high contrast optical testbed and exploring alternative techniques for improving our initial wavefront estimation. Due to its model-free approach and ease of implementation, iEFC through a SMF is a promising path forward for achieving high contrasts in future ground and space-based missions.

APPENDIX A. FIBER-BASED ELECTRIC FIELD CONJUGATION

We can define the electric field in the image plane as

$$E_{im} = C\left\{Ae^{i(\phi_{DM}+\phi_{ab})}\right\} \tag{12}$$

where C is the coronagraph operator, A is the pupil field, and ϕ_{DM} and ϕ_{ab} are the DM phase and optical system aberrations, respectively. Assuming $\phi_{DM} \approx \phi_{ab} << 1$ and using a 1st-order Taylor Series approximation for ϕ_{DM}, we can rewrite our expression for E_{im} as

$$E_{im} \approx C\left\{Ae^{i(\phi_{ab})}\right\} + iC\left\{A\phi_{DM}\right\} = E_{ab} + \delta E_{DM} \tag{13}$$

where E_{ab} represents the best estimate we have for E_{im} and δE_{DM} represents the error in our estimate.[10]

Now, we can express δE_{DM} as

$$\delta E_{DM} = \mathbf{G}\vec{u} \tag{14}$$

where $\mathbf{G}$ represents the Jacobian of the system with respect to the DM (N actuators by N pixels) and $\vec{u}$ represents the vector of changes in actuator heights. Thus, we obtain the expression

$$E_{im} = E_{ab} + \mathbf{G}\vec{u} \tag{15}$$

for our electric field at the image plane.

To estimate E_{im}, we take a series of intensity measurements at the image plane. We then modulate the DM surface to perturb E_{im}. These perturbations to E_{im} are referred to as "probes." We can express the measured intensity at the output of the single-mode fiber as

$$I = \left|\int (E_{ab} + \mathbf{G}\vec{u})\Psi_{SMF} da\right|^2 \tag{16}$$

$$= \left|\int \Psi_{SMF} E_{ab} da\right|^2 + \left|\int \Psi_{SMF}\mathbf{G}\vec{u} da\right|^2 + 2Re\left\{\int \Psi_{SMF} E_{ab} da \times \int \Psi_{SMF}\mathbf{G}\vec{u} da\right\} \tag{17}$$

Now, let us define one pair of probes as $E = \pm \mathbf{G}\vec{u}$. The intensity difference between the positive and negative probe images can be expressed as

$$\Delta I = 4Re\left\{\int \Psi_{SMF} E_{ab} da \times \int \Psi_{SMF} \mathbf{G}\vec{u} da\right\} \tag{18}$$

$$= 4\int \Psi_{SMF} Re\left\{E_{ab}\right\} da \int \Psi_{SMF} Re\left\{\mathbf{G}\vec{u}\right\} da \tag{19}$$

$$+4\int \Psi_{SMF} Im\left\{E_{ab}\right\} da \int \Psi_{SMF} Im\left\{\mathbf{G}\vec{u}\right\} da \tag{20}$$

For n pairs of probes, the above expression can be written as

$$\begin{bmatrix} \Delta I_1 \\ \vdots \\ \Delta I_n \end{bmatrix} = 4 \begin{bmatrix} \int \Psi_{SMF} Re\left\{\mathbf{G}\vec{u_1}\right\} da & \int \Psi_{SMF} Im\left\{\mathbf{G}\vec{u_1}\right\} da \\ \vdots & \vdots \\ \int \Psi_{SMF} Re\left\{\mathbf{G}\vec{u_n}\right\} da & \int \Psi_{SMF} Im\left\{\mathbf{G}\vec{u_n}\right\} da \end{bmatrix} \times \begin{bmatrix} \int \Psi_{SMF} Re\left\{E_{ab}\right\} da \\ \int \Psi_{SMF} Im\left\{E_{ab}\right\} da \end{bmatrix} \tag{21}$$

.

We can also express Equation (21) more simply as $\Delta I = \mathbf{H}s$ where we let $\mathbf{H}$ stand in for the complex conjugate matrix and s stand in for our aberrated electric field through the fiber. Because $\mathbf{H}$ is not square, we must take a pseudo inverse of $\mathbf{H}$ to find an estimate of the fibxel electric field. This can be expressed as

$$\hat{s} = \mathbf{H}^{\dagger} \Delta I \tag{22}$$

, where $\hat{s}$, specifically, is the estimate of the complex overlap integral. This estimate is computed at each control iteration.

Now that we have estimated the overlap integral of the electric field in the image plane, we can use a similar approach to that of conventional EFC.

ACKNOWLEDGMENTS

This work was supported by NASA SAT under award number 80NSSC20K0624.

REFERENCES

[1] Currie, T., Biller, B., Lagrange, A.-M., Marois, C., Guyon, O., Nielsen, E., Bonnefoy, M., and De Rosa, R., "Direct Imaging and Spectroscopy of Extrasolar Planets," *arXiv e-prints* , arXiv:2205.05696 (May 2022).

[2] Galicher, R. and Mazoyer, J., "Imaging exoplanets with coronagraphic instruments," *arXiv e-prints* , arXiv:2302.10833 (Feb. 2023).

[3] Pueyo, L., Stark, C., Juanola-Parramon, R., Zimmerman, N., Bolcar, M., Roberge, A., Arney, G., Ruane, G., Riggs, A. J., Belikov, R., Sirbu, D., Redding, D., Soummer, R., Laginja, I., and Will, S., "The LUVOIR Extreme Coronagraph for Living Planetary Systems (ECLIPS) I: searching and characterizing exoplanetary gems," in [*Society of Photo-Optical Instrumentation Engineers (SPIE) Conference Series*], *Society of Photo-Optical Instrumentation Engineers (SPIE) Conference Series* **11117**, 1111703 (Sept. 2019).

[4] Stahl, H. P., Kuan, G., Arnold, W., Baysinger, M., Brooks, T., Garcia, J., and Knight, J. B., "Habitable-zone observatory (HabEx) baseline 4-m telescope design and predicted performance," in [*Society of Photo-Optical Instrumentation Engineers (SPIE) Conference Series*], *Society of Photo-Optical Instrumentation Engineers (SPIE) Conference Series* **11443**, 114433C (Dec. 2020).

[5] Queloz, D., Mayor, M., Weber, L., Blécha, A., Burnet, M., Confino, B., Naef, D., Pepe, F., Santos, N., and Udry, S., "The CORALIE survey for southern extra-solar planets. I. A planet orbiting the star Gliese 86," **354**, 99–102 (Feb. 2000).

[6] Snellen, I., de Kok, R., Birkby, J. L., Brandl, B., Brogi, M., Keller, C., Kenworthy, M., Schwarz, H., and Stuik, R., "Combining high-dispersion spectroscopy with high contrast imaging: Probing rocky planets around our nearest neighbors," **576**, A59 (Apr. 2015).

[7] Mawet, D., Ruane, G., Xuan, W., Echeverri, D., Klimovich, N., Randolph, M., Fucik, J., Wallace, J. K., Wang, J., Vasisht, G., Dekany, R., Mennesson, B., Choquet, E., Delorme, J. R., and Serabyn, E., "Observing Exoplanets with High-dispersion Coronagraphy. II. Demonstration of an Active Single-mode Fiber Injection Unit," **838**, 92 (Apr. 2017).

[8] Delorme, J.-R., Jovanovic, N., Echeverri, D., Mawet, D., Kent Wallace, J., Bartos, R. D., Cetre, S., Wizinowich, P., Ragland, S., Lilley, S., Wetherell, E., Doppmann, G., Wang, J. J., Morris, E. C., Ruffio, J.-B., Martin, E. C., Fitzgerald, M. P., Ruane, G., Schofield, T., Suominen, N., Calvin, B., Wang, E., Magnone, K., Johnson, C., Sohn, J. M., López, R. A., Bond, C. Z., Pezzato, J., Sayson, J. L., Chun, M., and Skemer, A. J., "Keck Planet Imager and Characterizer: a dedicated single-mode fiber injection unit for high-resolution exoplanet spectroscopy," *Journal of Astronomical Telescopes, Instruments, and Systems* **7**, 035006 (July 2021).

[9] Kotani, T., Kawahara, H., Ishizuka, M., Jovanovic, N., Vievard, S., Lozi, J., Sahoo, A., Guyon, O., Yoneta, K., and Tamura, M., "Extremely high-contrast, high spectral resolution spectrometer REACH for the Subaru Telescope," in [*Society of Photo-Optical Instrumentation Engineers (SPIE) Conference Series*], *Society of Photo-Optical Instrumentation Engineers (SPIE) Conference Series* **11448**, 1144878 (Dec. 2020).

[10] Llop-Sayson, J., Ruane, G., Mawet, D., Jovanovic, N., Calvin, B., Levraud, N., Roberson, M., Delorme, J.-R., Echeverri, D., Klimovich, N., and Xin, Y., "Demonstration of an electric field conjugation algorithm for improved starlight rejection through a single mode optical fiber," *Journal of Astronomical Telescopes, Instruments, and Systems* **5**, 019004 (Jan. 2019).

[11] Coker, C. T., Shaklan, S. B., Riggs, A. J. E., and Ruane, G., "Simulations of a high-contrast single-mode fiber coronagraphic multiobject spectrograph for future space telescopes," *Journal of Astronomical Telescopes, Instruments, and Systems* **5**, 045003 (Oct. 2019).

[12] Llop-Sayson, J., Kappel, C., Jovanovic, N., Mawet, D., and Coker, C., "New method to achieve the proper polarization state for a vector vortex coronagraph," in [*Techniques and Instrumentation for Detection of Exoplanets X*], Shaklan, S. B. and Ruane, G. J., eds., *Society of Photo-Optical Instrumentation Engineers (SPIE) Conference Series* **11823**, 118230P (Sept. 2021).

[13] Xin, Y., Xuan, J. W., Mawet, D., Wang, J., Ruane, G., Echeverri, D., Jovanovic, N., Do Ó, C., Fitzgerald, M., Horstman, K., Hsu, C.-C., Liberman, J., López, R. A., Phillips, C. L., Ren, B. B., Ruffio, J.-B., and Sappey, B., "On-sky speckle nulling through a single-mode fiber with the Keck Planet Imager and Characterizer," *arXiv e-prints* , arXiv:2307.11893 (July 2023).

[14] Haffert, S. Y., Males, J. R., Ahn, K., Van Gorkom, K., Guyon, O., Close, L. M., Long, J. D., Hedglen, A. D., Schatz, L., Kautz, M., Lumbres, J., Rodack, A., Knight, J. M., and Miller, K., "Implicit electric field Conjugation: Data-driven focal plane control," *arXiv e-prints* , arXiv:2303.13719 (Mar. 2023).

[15] Groff, T. D., Eldorado Riggs, A. J., Kern, B., and Jeremy Kasdin, N., "Methods and limitations of focal plane sensing, estimation, and control in high-contrast imaging," *Journal of Astronomical Telescopes, Instruments, and Systems* **2**, 011009 (Jan. 2016).

[16] Kasdin, N. J., Bailey, V. P., Mennesson, B., Zellem, R. T., Ygouf, M., Rhodes, J., Luchik, T., Zhao, F., Riggs, A. J. E., Seo, B.-J., Krist, J., Kern, B., Tang, H., Nemati, B., Groff, T. D., Zimmerman, N., Macintosh, B., Turnbull, M., Debes, J., Douglas, E. S., and Lupu, R. E., "The Nancy Grace Roman Space Telescope Coronagraph Instrument (CGI) technology demonstration," in [*Space Telescopes and Instrumentation 2020: Optical, Infrared, and Millimeter Wave*], Lystrup, M. and Perrin, M. D., eds., *Society of Photo-Optical Instrumentation Engineers (SPIE) Conference Series* **11443**, 114431U (Dec. 2020).

[17] Give'on, A., Kern, B., Shaklan, S., Moody, D. C., and Pueyo, L., "Broadband wavefront correction algorithm for high-contrast imaging systems," in [*Astronomical Adaptive Optics Systems and Applications III*], Tyson, R. K. and Lloyd-Hart, M., eds., *Society of Photo-Optical Instrumentation Engineers (SPIE) Conference Series* **6691**, 66910A (Sept. 2007).

[18] Matthews, C. T., Crepp, J. R., Vasisht, G., and Cady, E., "Electric field conjugation for ground-based high-contrast imaging: robustness study and tests with the Project 1640 coronagraph," *Journal of Astronomical Telescopes, Instruments, and Systems* **3**, 045001 (Oct. 2017).

[19] Ahn, K., Guyon, O., Lozi, J., Vievard, S., Deo, V., Skaf, N., Bragg, J. C., Haffert, S. Y., Males, J. R., and Currie, T., "Combining EFC with spatial LDFC for high-contrast imaging on Subaru/SCExAO," *Astronomy & Astrophysics* (Mar. 2023). Publisher: EDP Sciences.

[20] Ruffio, J.-B. and Kasper, M., "Non Common Path Aberrations Correction," *arXiv e-prints* , arXiv:2211.00775 (Nov. 2022).

[21] Give'on, A., Kern, B. D., and Shaklan, S., "Pair-wise, deformable mirror, image plane-based diversity electric field estimation for high contrast coronagraphy," in [*Techniques and Instrumentation for Detection of Exoplanets V*], Shaklan, S., ed., *Society of Photo-Optical Instrumentation Engineers (SPIE) Conference Series* **8151**, 815110 (Oct. 2011).

[22] Llop-Sayson, J., Ruane, G., Jovanovic, N., Mawet, D., Echeverri, D., Riggs, A. J. E., Coker, C. T., Morrissey, G., and Sun, H., "The high-contrast spectroscopy testbed for segmented telescopes (HCST): new wavefront control demonstrations," in [*Society of Photo-Optical Instrumentation Engineers (SPIE) Conference Series*], *Society of Photo-Optical Instrumentation Engineers (SPIE) Conference Series* **11117**, 111171W (Sept. 2019).

[23] Riggs, A. J. E., Ruane, G., Sidick, E., Coker, C., Kern, B. D., and Shaklan, S. B., "Fast linearized coronagraph optimizer (FALCO) I: a software toolbox for rapid coronagraphic design and wavefront correction," in [*Space Telescopes and Instrumentation 2018: Optical, Infrared, and Millimeter Wave*], Lystrup, M., MacEwen, H. A., Fazio, G. G., Batalha, N., Siegler, N., and Tong, E. C., eds., *Society of Photo-Optical Instrumentation Engineers (SPIE) Conference Series* **10698**, 106982V (Aug. 2018).

[24] Mawet, D., Fitzgerald, M. P., Konopacky, Q., Jovanovic, N., Baker, A., Beichman, C., Bertz, R., Dekany, R., Fucik, J., Roberts, M., Porter, M., Pahuja, R., Ruane, G., Leifer, S., Halverson, S., Gibbs, A., Johnson, C., Kress, E., Magnone, K., Sohn, J. M., Wang, E., Brown, A., Maire, J., Sappey, B., Andersen, D., Terada, H., Kassis, M., Artigau, E., Benneke, B., Doyon, R., Kotani, T., Tamura, M., Beatty, T., Plavchan, P., Do, T., Nishiyama, S., Wang, J., and Wang, J., "Fiber-fed high-resolution infrared spectroscopy at the diffraction limit with Keck-HISPEC and TMT-MODHIS: status update," in [*Ground-based and Airborne Instrumentation for Astronomy IX*], Evans, C. J., Bryant, J. J., and Motohara, K., eds., *Society of Photo-Optical Instrumentation Engineers (SPIE) Conference Series* **12184**, 121841R (Aug. 2022).